# Dynamic Tracking of Power Demand for Integrated Fuel Cell Systems using Nonlinear Model Predictive Control [★]

**Verena Neisen** [∗], **Jacob Mannhardt** [∗], **Dirk Abel** [∗]

[∗] *Institute of Automatic Control, RWTH Aachen University, 52074 Aachen, Germany (e-mail: v.neisen@irt.rwth-aachen.de).*

**Abstract:** Transient changes in the power demand of state-of-the-art fuel cell systems are compensated by a battery in order to operate the fuel cell system safely within its physical boundaries. More concretely, oxygen starvation in the fuel cell is conventionally prevented by directly controlling the oxygen excess ratio. However, this limits the transient response of the fuel cell and the system's overall flexibility and efficiency. In order to overcome these limitations, we ascribe the task of the dynamic but safe response in a hybrid system to the fuel cell. For this purpose, we present a nonlinear model predictive control approach which is able to realize efficient transient power tracking, while considering the oxygen excess ratio explicitly as a boundary. We address the control challenges of a nonlinear, coupled, and bounded system with an adequate control design using a real-time capable nonlinear controller model. The controller is validated as proof of concept in simulation with a detailed dynamic plant model. Our contribution realizes a collaborative power setting by fuel cell and compressor. Moreover, system efficiency both in stationary and in transient operation is achieved, while preventing oxygen starvation as well as compressor surge and choke throughout the entire operation.

*Keywords:* Fuel cell systems, Air-path control, Model-based control, Nonlinear systems

## 1. INTRODUCTION

Fuel cell systems have recently become one of the most promising technologies for emission-free power generation both in stationary and mobile applications. This development can be attributed to their wide applicability, high power density and efficient operation (Gruber et al., 2012). In order to further exploit their potential in clean power production, a safe but increasingly dynamic and powerful operation of fuel cells is desired (Pukrushpan et al., 2004; Li and Liu, 2009).

The central issues of a dynamic power supply are its compliance with physical boundaries, power demand tracking, and system efficiency. These issues are determined and dominated by the cathodic air path including the compressor (Pukrushpan et al., 2004), which is part of a periphery with a variety of components (see Fig. 1). Hence, the focus of this paper lies on the cathodic air dynamics.

Yet, the dynamic operation and transient response of fuel cell systems are predominantly considered slow (Li and Liu, 2009). This is because such systems are challenging to control, especially during transients: The system of interest is over-actuated with coupled, nonlinear, and constrained system dynamics (Ettihir et al., 2016). Oxygen starvation in the fuel cell, as the most critical boundary, threatens the functionality and lifecycle of the fuel cell stack (Guo et al., 2013). Especially during load changes, fuel cells are prone to oxygen starvation, since the dy-
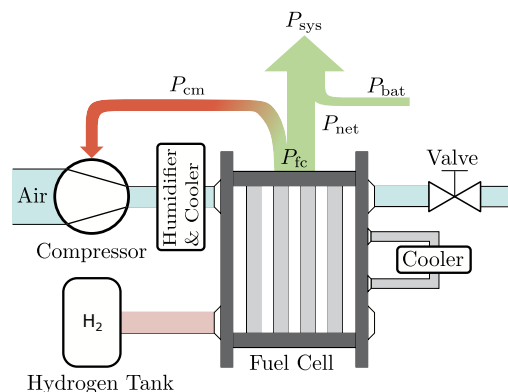


Fig. 1. Schematic structure of the integrated fuel cell system as part of a hybrid system, and power flows of the overall system $P_{sys}$, the battery $P_{bat}$, the fuel cell stack $P_{fc}$ and the compressor $P_{cm}$, resulting in the fuel cell system net power $P_{net}$.

namics of the reactant-supplying air flow are significantly slower than the reactant-consuming electrochemistry. Consequently, many contributions operate the fuel cell conservatively and hence extensively use a secondary component, such as batteries or supercapacitors, to buffer the transient power delay during these load changes (Liu et al., 2018; Ettihir et al., 2016; Li and Liu, 2009; Vahidi et al., 2006). In contrast, we investigate a control approach which ascribes the task of dynamic power supply in a hybrid system to the fuel cell while adhering to the boundaries. As one beneficial consequence, the secondary component can be downsized.

As another challenge of dynamic power supply, starvation prevention at all times is considered to be more important than an instantaneous and efficient power setting. Hence, many contributions treat the oxygen excess ratio $\lambda_{O_2}$ as the primary control objective. It is often chosen as the main control variable and maintained at $\lambda_{O_2,\mathrm{dem}} = 2$ without explicit consideration of an efficient system operation (Vahidi et al., 2006; Bordons et al., 2006; Puig et al., 2007; Gruber et al., 2012). Other contributions propose tracking an efficiency maximized steady-state excess ratio $\lambda_{O_2,\mathrm{dem}}^*$, which is subject to the operation point and thereby still confines the range of the system operation more strictly than necessary (Guo et al., 2013; Bordons et al., 2006; Arce et al., 2010; Hähnel et al., 2015). In contrast, we omit the control of $\lambda_{O_2}$ but consider oxygen starvation explicitly as a boundary. We thereby create the potential to treat the power demand tracking and efficiency as the primary control objectives.

The omission of the safety-focused control variable necessitates accurate knowledge of system dynamics and states, and, most importantly, the ability to explicitly consider boundaries in the controller. For this purpose, model predictive control (MPC) strategies are predestined to be applied to the system of interest (Vahidi et al., 2006; Bordons et al., 2006; Gruber et al., 2012; Arce et al., 2010; Hähnel et al., 2015; Liu et al., 2018). While the majority of presented solutions use a linearized approximation in the operation point (Arce et al., 2010; Bordons et al., 2006), the accurate prediction of system dynamics is essential during transients in the presence of physical boundaries, and hence a nonlinear description and thus nonlinear MPC (NMPC) is beneficial, as presented in this paper.

Considering efficiency and power tracking in detail, the compressor accounts for the highest peripheral power consumption and the dominant time lag. On the one hand, the compressor operation lowers the overall efficiency of the fuel cell system by up to $30\,\%$ (Haubrock et al., 2006). Thus, it is sought to be reduced to a minimum. On the other hand, the system's net power $P_{\mathrm{net}}$ is jointly determined by the fuel cell $P_{\mathrm{fc}}$ and the compressor $P_{\mathrm{cm}}$, as shown in Fig. 1. Simultaneously, neither $P_{\mathrm{cm}}$ nor $P_{\mathrm{fc}}$ can follow step-like load changes without deviation due to their delayed transient response. Yet collaboratively, dynamic delay can be eliminated and an accurate dynamic power tracking can be achieved. Thus far, $P_{\mathrm{cm}}$ is widely considered solely parasitic and hence, the potential of the over-actuated system of fuel cell stack and compressor is not utilized (Pukrushpan et al., 2004; Haubrock et al., 2006; Suh and Stefanopoulou, 2006; Zhao et al., 2016). In contrast, we include both $P_{\mathrm{cm}}$ and $P_{\mathrm{fc}}$ as an additional degree of freedom in the control strategy. Hence, we promote an efficient and deviation-free power demand tracking in both transient and steady state. To the best of our knowledge, this has not yet been of research interest.

In this contribution, we present an NMPC with power reference tracking and efficiency optimization for the fuel cell system. Hence, the power of both the fuel cell $P_{\mathrm{fc}}$ and the compressor $P_{\mathrm{cm}}$ is considered and the reference $P_{\mathrm{net,dem}}$ hence collaboratively set. Simultaneously, compliance with all physical boundaries, i.e. starvation prevention as well as choke and surge prevention in the compressor, is ensured. We omit all optimization objectives which solely seek to

keep the operation physically valid and reformulate them as boundaries. We thereby enable the fuel cell system to a more dynamic and powerful operation.

The paper is organized as follows. In Sec. 2, the control approach for the fuel cell system in the context of a hybrid system is described, including the controller model deduction. The control design is described in Sec. 3. Finally, the application of the controller to a detailed plant model is presented in Sec. 4 and the control performance is evaluated. A conclusion is drawn in Sec. 5.

## 2. CONTROL-ORIENTED MODELING

In this section, we present the plant model and the variables, followed by the general prediction model simplifications (reduced-order model) with focus on the cathodic air flow. Subsequently, the prediction model is summarized by a system of nonlinear differential equations.

*Plant Model* Figure 2 depicts the plant model of the integrated proton exchange membrane fuel cell (PEM FC) system, used in this paper as part of a hybrid system with a battery and power electronics. The fuel cell system model is obtained from the detailed dynamic model by Pukrushpan et al. (2004), which is widely recognized for its comprehensiveness and wide range of applicability. For conciseness of this paper, we refrain from restating the overall system model and focus on simplifications and modified equations. The complete dynamic model can be accessed as a MATLAB/Simulink® model in Pukrushpan et al. (2002).
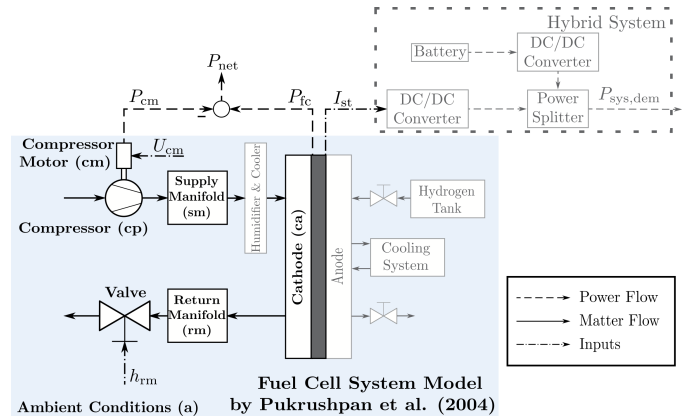


Fig. 2. Schematic structure of the plant model of the PEM fuel cell system - black: considered in controller model, grey: neglected in controller model.

*Controller Variables* We choose the *states* $\mathbf{x} = (p_{\mathrm{ca}}, p_{\mathrm{rm}}, p_{O_2}, p_{\mathrm{sm}}, \omega_{\mathrm{cp}}, m_{\mathrm{sm}}, T_{\mathrm{st}}, U_{\mathrm{fc}})$, with the pressure in the cathode $p_{\mathrm{ca}}$ and in the return manifold $p_{\mathrm{rm}}$, the oxygen partial pressure in the cathode $p_{O_2}$, the pressure in the supply manifold $p_{\mathrm{sm}}$, the compressor speed $\omega_{\mathrm{cp}}$, the air mass in the supply manifold $m_{\mathrm{sm}}$, the stack temperature $T_{\mathrm{st}}$, and the stack voltage $U_{\mathrm{fc}}$. The *inputs* $\mathbf{u} = (I_{\mathrm{st}}, U_{\mathrm{cm}}, h_{\mathrm{rm}})$ are analogous to Vahidi et al. (2006) the fuel cell current $I_{\mathrm{st}}$ and compressor voltage $U_{\mathrm{cm}}$. Furthermore, we add the aperture of the valve $h_{\mathrm{rm}}$ as a further input in order to obtain a degree of freedom in the compressor operation (Hähnel et al., 2015). The *output* is $\mathbf{y} = P_{\mathrm{net}}$.

## 2.1 General Modeling

The controller model is derived from the plant model with regard to the following key aspects:

I) dynamic power tracking,
II) compressor surge and choke prevention,
III) prevention of oxygen starvation, and
IV) efficiency maximization in transient and steady state.

*Fuel Cell Voltage Formation*    The core of the fuel cell system model is the nonlinear voltage formation $U_{fc}$ of the fuel cell, with the Nernst potential $U_n$, corrected by the three voltage losses $\Delta U_{act}$, $\Delta U_{ohm}$, and $\Delta U_{diff}$:

$$U_{fc} = U_n - \Delta U_{act} - \Delta U_{ohm} - \Delta U_{diff} \tag{1}$$
$$= f(p_{ca}, p_{O_2}, T_{st}, I_{st}).$$
$$P_{fc} = I_{st} U_{fc} \tag{2}$$

As $U_{fc}$ determines the fuel cell power $P_{fc}$, it is crucial for the control performance and hence modeled identical to the plant model.

We assume the following simplifications with subordinate relevance to the key aspects (I–IV). Figure 2 depicts the considered components in black and the neglected elements in grey. We assume that the compressor is the only power consuming auxiliary component (Haubrock et al., 2006; Liu et al., 2018). Thus, the net power $P_{net}$ is calculated as the difference between $P_{fc}$ and the compressor power $P_{cm}$ (Pukrushpan et al., 2004):

$$P_{net} = P_{fc} - P_{cm}. \tag{3}$$

Since this paper's focus lies on the cathodic dynamics, no anodic effects, such as purging, are modeled. Active cooling is ignored, since its effect on the temperature formation over the prediction horizon is small. Moreover, we assume an ideal humidifier and thus neglect the influence of humidity (Hähnel et al., 2015). Finally, the pressure balancing between anode and cathode as well as the stack cooling are not considered in the NMPC. Instead, auxiliary PID controllers are ascribed with these tasks, as proposed by e.g. Vahidi et al. (2006).

## 2.2 Cathodic Air Flow Modeling

All key aspects of the control (I–IV) concern the cathodic air flow. Consequently, the controller model includes the essential physics of the compressor and the flows through the three control volumina (**sm**, **ca**, **rm** (see Fig. 2)):

*Compressor*    The electrical power consumption of the compressor $P_{cm}$ is calculated by:

$$P_{cm} = \frac{U_{cm}}{R_{cm}}(U_{cm} - k_v \omega_{cp}), \tag{4}$$

with the compressor motor voltage $U_{cm}$ and the motor constants $R_{cm} = 0.82 \ \Omega$ and $k_v$. The compressor speed $\omega_{cp}$ is obtained via conservation of momentum $\tau_i$ with the compressor inertia $J_{cp} = 5 \cdot 10^{-5} \ \mathrm{kg/m^2}$:

$$\frac{d\omega_{cp}}{dt} = \frac{1}{J_{cp}}(\tau_{cm} - \tau_{cp}) \tag{5}$$

$$\tau_{cm} = \eta_{cm} \frac{k_t P_{cm}}{U_{cm}} \tag{6}$$

$$\tau_{cp} = \frac{c_p T_a}{\omega_{cp} \eta_{cp}}\left(\Pi^{\frac{\gamma-1}{\gamma}} - 1\right)\dot{m}_{cp}, \tag{7}$$



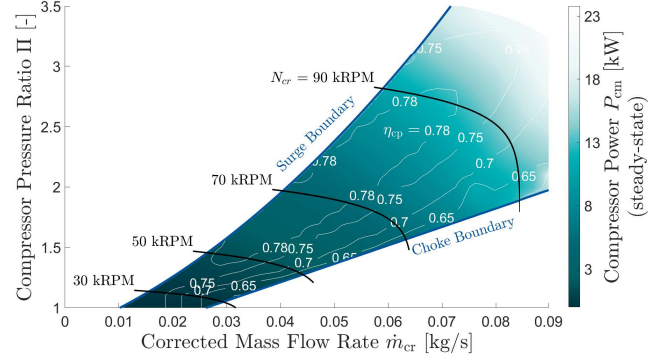Fig. 3. Compressor map.

Table 1. Parameters $\delta_{ij}$ of compressor mass flow rate approximation $\dot{m}_{cr}$.

| | | | |
|---|---|---|---|
| $\delta_{00}$ | $1.96 \cdot 10^{-1} \ \frac{kg}{s}$ | $\delta_{10}$ | $-9.98 \cdot 10^{-2} \ \frac{kg}{s}$ |
| $\delta_{20}$ | $-9.47 \cdot 10^{-2} \ \frac{kg}{s}$ | $\delta_{11}$ | $4.81 \cdot 10^{-6} \ \frac{kg}{s\,(RPM)}$ |
| $\delta_{21}$ | $6.09 \cdot 10^{-7} \ \frac{kg}{s\,(RPM)}$ | $\delta_{12}$ | $-2.08 \cdot 10^{-11} \ \frac{kg}{s\,(RPM)^2}$ |
| $\delta_{01}$ | $-4.73 \cdot 10^{-6} \ \frac{kg}{s\,(RPM)}$ | $\delta_{02}$ | $4.36 \cdot 10^{-11} \ \frac{kg}{s\,(RPM)^2}$ |
| $\delta_{03}$ | $-2.87 \cdot 10^{-16} \ \frac{kg}{s\,(RPM)^3}$ | $\delta_{13}, \delta_{22}, \delta_{23}$ | $= 0$ |

with the compressor motor efficiency $\eta_{cm} = 0.98$, the motor constant $k_t = k_v = 0.0153 \ \mathrm{Nm/A}$, the heat capacity ratio of air $\gamma = c_p/c_v = 1.4$, the ambient temperature $T_a$, the pressure ratio across the compressor $\Pi = p_{sm}/p_a$ with the ambient pressure $p_a$. The variable compressor flow efficiency $\eta_{cp} = f(\dot{m}_{cp}, p_{sm})$ in the plant model, is set to a constant value of $\eta_{cp} = 0.8$ in the controller model. As a result, the computational effort is reduced while accepting a minor mismatch. The compressor mass flow rate $\dot{m}_{cp}$ is obtained from the compressor map (see Fig. 3 and (8)) via the corrected compressor mass flow $\dot{m}_{cr} = f(\Pi, (N_{cr} \propto \omega_{cp}))$, with the temperature correction ($\Theta = \sqrt{T_a/288K}$) and pressure correction ($\psi = p_a/1\mathrm{atm}$). In the plant model, the compressor map is approximated by an exponential equation for $\dot{m}_{cr}$, which is computationally intensive with high gradients in the operation area's periphery, and can cause numerical instabilities within the control algorithm. Thus, we calculate a polynomial fit for the controller model of the NMPC using a least squares fit:

$$\dot{m}_{cp} = \frac{\psi}{\Theta}\dot{m}_{cr} \approx \frac{\psi}{\Theta}\sum_{i=0}^{2}\sum_{j=0}^{3}\delta_{ij}\Pi^i N_{cr}^j. \tag{8}$$

The parameters $\delta_{ij}$ are listed in Tab. 1. Inadequate approximation might lead to an operation outside the boundaries. Especially in surge operation, this can cause severe damage to the compressor and the entire air flow system (Kurz et al., 2016). Thus, it is of utmost importance that the polynomial approximation shows little deviation from the exponential equation in vicinity to the surge and choke boundary, so that the controller can obey the boundaries correctly. Therefore, the weight of the value points for the approximation is raised in proximity to the surge and choke line.

*Manifold and Cathode Connections*    In comparison to the original plant model, the connections between the inlet manifold and cathode, respectively cathode and return manifold were changed from nozzles to orifices. Nozzles

are in general intended to control a flow, while orifices can result from a constructional necessity. The mass flow across an orifice $\dot{m}_{\mathrm{ori}}$ can be described as:

$$\dot{m}_{\mathrm{ori}} = \alpha \, A \, \rho_{\mathrm{A}} \sqrt{2 \frac{\Delta p}{\rho_{\mathrm{A}}}}, \qquad (9)$$

where $\alpha = 0.3$ is the flow coefficient, $A$ the orifice area, $\rho_{\mathrm{A}}$ the density of air before the orifice and $\Delta p$ the pressure loss across the orifice (Hähnel et al., 2015). The orifice area $A$ is empirically derived ($A_{\mathrm{ca,in}} = 0.0003\,\mathrm{m}^2$, $A_{\mathrm{ca,out}} = 0.00025\,\mathrm{m}^2$), so that the ratio between $\dot{m}_{\mathrm{ori}}$ and $\Delta p$ approximates the nozzle parameter $k$ used in the original model by Pukrushpan et al. (2004). It can be observed that this formulation slows down the air flow dynamics, and hence stabilizes the cathodic air flow.

Inspired by Hähnel et al. (2015), we substitute the return manifold's nozzle by a valve (10), i.e. expand the nozzle equation by an aperture $h_{\mathrm{rm}} = \dot{m}_{\mathrm{v}}/\dot{m}_{\mathrm{v,max}}$, which indicates the valve's relative flow rate. The maximum mass flow across the valve $\dot{m}_{\mathrm{v,max}}$ equals a linearized nozzle mass flow (Pukrushpan et al., 2004). $k_{\mathrm{rm}} = 5 \cdot 10^{-6}\,\mathrm{kg}/(\mathrm{s\,Pa})$ is the nozzle parameter.

$$\dot{m}_{\mathrm{v}} = \dot{m}_{\mathrm{v,max}} \, h_{\mathrm{rm}} = k_{\mathrm{rm}}(p_{\mathrm{rm}} - p_{\mathrm{a}}) \, h_{\mathrm{rm}} \qquad (10)$$

### 2.3 Overall State-Space Model

The resulting prediction model of the fuel cell system is mathematically described by the state-space model as a system of nonlinear ordinary differential equations (ODE) and the output equation:

$$\dot{\mathbf{x}} = f(\mathbf{x}, \mathbf{u}) \qquad (11a)$$
$$\mathbf{y} = g(\mathbf{x}, \mathbf{u}). \qquad (11b)$$

The entirety of state and output equations is modeled via ideal gas law, mole flows $\dot{n}_{\mathrm{i}}$, mass flows $\dot{m}_{\mathrm{i}}$, constants $c_{\mathrm{i}}$, and conservation of energy (heat $\dot{Q}_{\mathrm{i}}$, power $P_{\mathrm{i}}$), momentum $\tau_{\mathrm{i}}$, and mass $m_{\mathrm{i}}$, according to Pukrushpan et al. (2004). The interconnections in the state-space model are:

$$\dot{p}_{\mathrm{ca}} = \dot{x}_1 = c_1 \sum \dot{m}_{\mathrm{i}} T_{\mathrm{st}} = f(p_{\mathrm{ca}}, p_{\mathrm{rm}}, p_{\mathrm{sm}}, T_{\mathrm{st}}, I_{\mathrm{st}}) \quad (12a)$$

$$\dot{p}_{\mathrm{rm}} = \dot{x}_2 = c_2 \sum \dot{m}_{\mathrm{i}} T_{\mathrm{st}} = f(p_{\mathrm{ca}}, p_{\mathrm{rm}}, T_{\mathrm{st}}, h_{\mathrm{rm}}) \quad (12b)$$

$$\dot{p}_{\mathrm{O}_2} = \dot{x}_3 = c_3 \sum \dot{n}_{\mathrm{i}} T_{\mathrm{st}} = f(p_{\mathrm{ca}}, p_{\mathrm{rm}}, ... \quad (12c)$$
$$p_{\mathrm{O}_2}, p_{\mathrm{sm}}, T_{\mathrm{st}}, I_{\mathrm{st}})$$

$$\dot{p}_{\mathrm{sm}} = \dot{x}_4 = c_4 \sum \dot{m}_{\mathrm{i}} T_{\mathrm{i}} = f(p_{\mathrm{ca}}, p_{\mathrm{sm}}, \omega_{\mathrm{cp}}, m_{\mathrm{sm}}) \quad (12d)$$

$$\dot{\omega}_{\mathrm{cp}} = \dot{x}_5 = c_5 \sum \tau_{\mathrm{i}} = f(p_{\mathrm{sm}}, \omega_{\mathrm{cp}}, m_{\mathrm{sm}}, U_{\mathrm{cm}}) \quad (12e)$$

$$\dot{m}_{\mathrm{sm}} = \dot{x}_6 = \sum \dot{m}_{\mathrm{i}} = f(p_{\mathrm{ca}}, p_{\mathrm{sm}}, \omega_{\mathrm{cp}}) \quad (12f)$$

$$\dot{T}_{\mathrm{st}} = \dot{x}_7 = c_7 \sum \dot{Q}_{\mathrm{i}} = f(T_{\mathrm{st}}, U_{\mathrm{fc}}, I_{\mathrm{st}}) \quad (12g)$$

$$\dot{U}_{\mathrm{fc}} = \dot{x}_8 = c_8 \left(U_{\mathrm{fc,mod}} - U_{\mathrm{fc}}\right) \quad (12h)$$
$$= f(p_{\mathrm{ca}}, p_{\mathrm{O}_2}, T_{\mathrm{st}}, U_{\mathrm{fc}}, I_{\mathrm{st}})$$

$$P_{\mathrm{net}} = y = \sum P_{\mathrm{i}} = g(\omega_{\mathrm{cp}}, U_{\mathrm{fc}}, I_{\mathrm{st}}, U_{\mathrm{cm}}). \quad (12i)$$

Note that in (12h) the fuel cell voltage $U_{\mathrm{fc}}$ is fed back to the controller as an artificial differential state via a first-order lag element in order to detect and correct mismatches between the plant and the controller model. The constant $c_8 = 1/\Delta t$ equals the inverse of the sampling time $\Delta t$. The

voltage $U_{\mathrm{fc}}$ is measured in the plant model and fed back to the controller every execution step. $U_{\mathrm{fc,mod}}$ is the stack voltage which is algebraically modeled in the controller model (Pukrushpan et al., 2004). Mismatches occur since the fuel cell voltage formation in the plant model is highly nonlinear and influenced by a multitude of variables that are regarded in a simplied manner in the controller model.

## 3. CONTROL DESIGN

This section presents the control design with the control structure, the optimal control problem (OCP), and the solver setup.
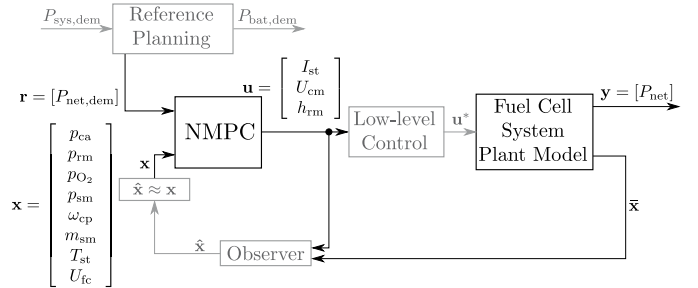
### 3.1 Control structure

Fig. 4. Schematic control structure with detailed dynamic plant model and NMPC including *states* $\mathbf{x}$, *inputs* $\mathbf{u}$, *outputs* $\mathbf{y}$ and the *reference* $\mathbf{r}$. The elements necessary for real-life application, i.e. reference planning, low-level control and state observer, are neglected in this paper and thus depicted in grey.

The control structure is schematically shown in Fig. 4. It depicts the resulting *states* $\mathbf{x}$ of the NMPC, the *inputs* $\mathbf{u}$, and the *output* $\mathbf{y} = P_{\mathrm{net}}$, which tracks the *reference* $\mathbf{r} = P_{\mathrm{net,dem}}$. We assume to follow a reference trajectory with prior knowledge of $P_{\mathrm{net,dem}}$ for the fuel cell system, as presented by Liu et al. (2018) and Hähnel et al. (2015). This is the case, if the controller is part of a hierarchical structure, in which the reference is generated by a reference planning optimization (Neisen et al., 2018; Liu et al., 2018). Hereby, we utilize predictive information in order to further exploit the advantages of MPC.

The *inputs* $\mathbf{u}$ are assumed to be set by a low-level control within a negligible bandwidth for the NMPC. $I_{\mathrm{st}}$ is assumed to be set by a DC/DC converter set-up, according to Bocklisch et al. (2010), which is simultaneously controlling the bus voltage at the DC-bus. For a proof of concept of the control performance, we assume perfect state knowledge. In the light of real-life application, a state observer will become necessary for stationary accuracy, and in order to estimate states which are not exactly measurable. Here, $m_{\mathrm{sm}}$ and $p_{\mathrm{O}_2}$ are the most difficult to measure. Though, $m_{\mathrm{sm}}$ can be calculated using the ideal gas law and mass balances. Furthermore, measurement methods for $p_{\mathrm{O}_2}$ already exist (Inukai et al., 2008).

### 3.2 Optimal Control Problem

The nonlinear optimal control problem (OCP) used in the NMPC is formulated as a minimization problem:

$$\min_{\mathbf{u}} \ J(\mathbf{x}, \mathbf{u}, \mathbf{x}_0, t) \qquad \text{cost function} \quad (13)$$
$$\text{s.t. } \dot{\mathbf{x}}(t) = f(\mathbf{x}, \mathbf{u}, t) \quad \text{system dynamics} \ (12)$$
$$\mathbf{x}(t_0) = \mathbf{x}_0 \qquad \text{initial value}$$
$$\mathbf{h}(\mathbf{x}, \mathbf{u}, t) \le \mathbf{0} \qquad \text{inequality constraints} \ (15)$$
$$\mathbf{u} \in [\mathbf{u}_{\min}, \mathbf{u}_{\max}] \quad \text{box constraints} \ (18).$$

*Cost Function*    The objective of this control is to minimize the deviation of the net power $P_{\text{net}}$ from a demanded reference power $P_{\text{net,dem}}$, while simultaneously maximizing the fuel cell system's efficiency $\eta_{\text{net}}$. Since we focus on a highly dynamic operation, efficiency maximization is desired in transient and steady state. This can be realized by formulating an additional, economic cost term. Pure reference tracking strategies, on the other hand, might fall short on reaching high transient efficiency, because they do not consider efficiency during load transitions (Ellis et al., 2014). We present a combination of a reference tracking MPC and an economic MPC. Accordingly, the cost function $J$ is designed as combination of a reference tracking functional $l_{\text{ref}}$ and an economic functional $l_{\text{e}}$. The optimization objectives are balanced by the weighting factors $q_{\text{ref}} = 1$ and $q_{\text{e}} = 0.45$.

$$J = \int_{t_0}^{t_0+T_{\text{h}}} [l_{\text{ref}}(\mathbf{x}, \mathbf{u}, t) + l_{\text{e}}(\mathbf{x}, \mathbf{u}, t)] \ \mathrm{d}t$$
$$= \int_{t_0}^{t_0+T_{\text{h}}} \Bigg[ \underbrace{q_{\text{ref}} \left( \frac{P_{\text{net}} - P_{\text{net,dem}}}{P_{\text{net,dem}}} \right)^2}_{l_{\text{ref}}(\mathbf{x}, \mathbf{u}, t)} + \underbrace{q_{\text{e}} \frac{I_{\text{st}}/I_{st,0}}{P_{\text{net}}}}_{l_{\text{e}}(\mathbf{x}, \mathbf{u}, t)} \Bigg] \ \mathrm{d}t \, . \quad (13)$$

$l_{\text{ref}}(\mathbf{x}, \mathbf{u}, t)$ is formulated as a normalized mean square minimization of the deviation from the demanded reference power $\mathbf{r} = P_{\text{net,dem}}$. The values of $P_{\text{net,dem}}$ are known to the controller at $t = t_0$ for the duration of the prediction horizon $T_{\text{h}}$. Hence, the response to a load change can be prepared prior to the actual event.

$l_e(\mathbf{x}, \mathbf{u}, t)$ is the normalized fuel consumption. It results from maximizing the fuel cell system efficiency $\eta_{\text{net}}$, which is equivalent to the minimum of its inverse:

$$\max \eta_{\text{net}} = \max \frac{P_{\text{net}}}{P_{\text{H}_2}} \Leftrightarrow \min \frac{1}{\eta_{\text{net}}} \underset{(P_{\text{H}_2} \propto I_{\text{st}})}{\Leftrightarrow} \min \frac{I_{\text{st}}}{P_{\text{net}}} . \quad (14)$$

$P_{\text{H}_2}$ is the consumed hydrogen power, which is, based on Faraday's Law, proportional to the fuel cell stack current $I_{\text{st}}$ (Pukrushpan et al., 2004), and thus the minimization of $P_{\text{H}_2}$ is equivalent to the minimization of $I_{\text{st}}$. $I_{\text{st},0}$ denotes the scaling value of $I_{\text{st}}$, as described in Sec. 3.3.

*Constraints*    The system dynamics are limited by essential operation restrictions, which are implemented as normalized inequality constraints in order to ameliorate the controller performance, and are described subsequently:

$$\mathbf{h}(\mathbf{x}, \mathbf{u}, t) = \begin{bmatrix} (p_{\text{ca,min}} - p_{\text{ca}})/\bar{p}_{\text{ca}} \\ (p_{\text{ca}} - p_{\text{ca,max}})/\bar{p}_{\text{ca}} \\ (\lambda_{\text{O}_2,\text{min}} - \lambda_{\text{O}_2})/\lambda_{\text{O}_2,\text{min}} \\ \Pi - 278.69 \, \dot{m}_{\text{cr}}^2 - 17.88 \, \dot{m}_{\text{cr}} - 0.79 \\ -\Pi + 15.27 \, \dot{m}_{\text{cr}} + 0.6 \end{bmatrix} \le \mathbf{0}. \quad (15)$$

with $\bar{p}_{\text{ca}} = (p_{\text{ca,min}} + p_{\text{ca,max}})/2$. They concern the cathode pressure $p_{\text{ca}}$, the oxygen excess ratio $\lambda_{\text{O}_2}$ and the surge

and choke boundaries of the compressor $\dot{m}_{\text{cr}} = f(\Pi, N_{\text{cr}})$. $\lambda_{\text{O}_2}$ is the ratio between the oxygen mass flow entering the cathode $\dot{m}_{\text{O}_2,\text{in}}$ and the consumed oxygen mass flow $\dot{m}_{\text{O}_2,\text{con}}$ (Pukrushpan et al., 2004):

$$\lambda_{\text{O}_2} = \frac{\dot{m}_{\text{O}_2,\text{in}}}{\dot{m}_{\text{O}_2,\text{con}}(I_{\text{st}})} = \frac{\dot{m}_{\text{ca,in}} \, w_{\text{O}_2}}{\dot{m}_{\text{O}_2,\text{con}}(I_{\text{st}})}. \quad (16)$$

The air mass flow entering the cathode $\dot{m}_{\text{ca,in}}$ is the mass flow across the orifice between supply manifold and cathode, and hence calculated with (9). The oxygen mass fraction of air $w_{\text{O}_2}$ is assumed constant and equal to that of the ambient air $w_{\text{O}_2} = 0.231$. $\dot{m}_{\text{O}_2,\text{con}}$ is proportional to $I_{\text{st}}$, based on Faraday's Law. The oxygen excess ratio $\lambda_{\text{O}_2}$ is kept above $\lambda_{\text{O}_2} \ge \lambda_{\text{O}_2,\text{min}} = 1.5$ (Puig et al., 2007). The cathode pressure is sought to remain within $1.013 \, \text{bar} = p_{\text{ca,min}} \le p_{\text{ca}} \le p_{\text{ca,max}} = 5 \, \text{bar}$.

The surge and choke boundaries, shown in Fig. 3, are obtained from Pukrushpan et al. (2004). Vahidi et al. (2006) linearizes both boundaries to use them in a linear MPC. In this paper, the original quadratic surge boundary is approximated with a second order least square fit, as this allows a broader operation at low pressure ratios:

$$\text{Surge}: \qquad \Pi \le 278.69 \, \dot{m}_{\text{cr}}^2 + 17.88 \, \dot{m}_{\text{cr}} + 0.79 \quad (17\text{a})$$
$$\text{Choke}: \qquad \Pi \ge 15.27 \, \dot{m}_{\text{cr}} + 0.6. \quad (17\text{b})$$

The inputs $\mathbf{u}$ are limited by box constraints typical for such fuel cell systems:

$$\underbrace{\begin{bmatrix} 25 \, \text{A} \\ 0 \, \text{V} \\ 0.008 \end{bmatrix}}_{\mathbf{u}_{\min}} \le \underbrace{\begin{bmatrix} I_{\text{st}} \\ U_{\text{cm}} \\ h_{\text{rm}} \end{bmatrix}}_{\mathbf{u}} \le \underbrace{\begin{bmatrix} 450 \, \text{A} \\ 400 \, \text{V} \\ 1 \end{bmatrix}}_{\mathbf{u}_{\max}}. \quad (18)$$

$I_{\text{st}}$ has a lower bound $I_{\text{st,min}} > 0$ in order to avoid high voltage gradients in the fuel cell. It is assumed that the outlet valve cannot be closed entirely, hence $h_{\text{rm}} \ge 0.008$ (Hähnel et al., 2015).

*3.3 Solver Setup*

The OCP in Sec. 3.2 is solved with the toolbox GRAMPC by Englert et al. (2019), which contains an outer augmented Lagrangian approach and an inner projected gradient method. The augmented lagrangian method replaces the constrained OCP with its unconstrained dual optimization problem, i.e. penalty parameters and multipliers are used to rephrase the constraints as an additional cost functional. The maximum iterations of the gradient method are set to $N_{\text{grad}} = 12$ and of the the augmented lagrangian method are set to $N_{\text{lag}} = 8$. The execution rate of the NMPC equals the sampling rate of the OCP within the prediction and leads to a sampling time $\Delta t = 25 \, \text{ms}$. In combination with the prediction horizon of $T_{\text{h}} = 1 \, \text{s}$, this results in $N_{\text{int}} = 41$ integration steps per execution of the NMPC. While other algorithms such as interior point methods typically show faster convergence, augmented lagrangian approaches are superior in rapidly finding a valid suboptimal solution, which is an important property for nonlinear OCPs (Englert et al., 2019).

Note that we do not penalize input gradients $\Delta \mathbf{u}$ in the cost function, since this might lower the inputs' dynamic response. Instead, we adjust the parameters of the solver, e.g. of the line search algorithm, in order to smoothen the inputs $\mathbf{u}(t)$. Though, we acknowledge that such input
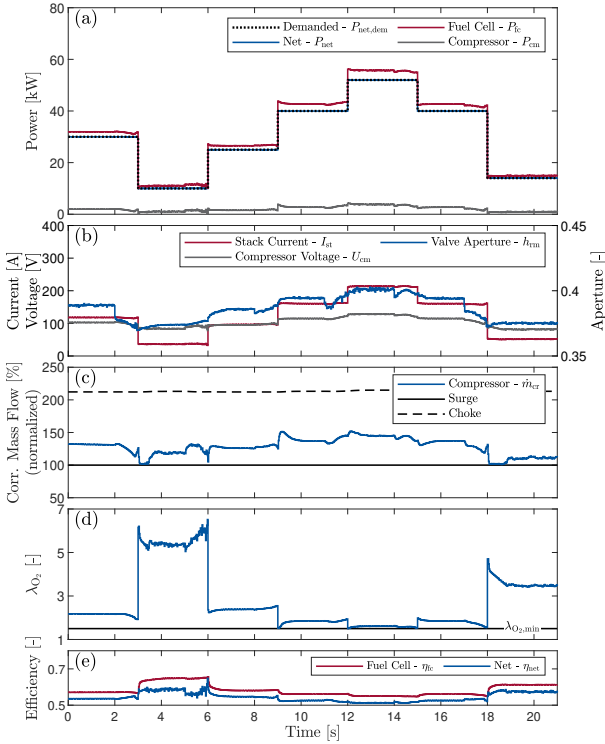
Fig. 5. Controlled systems response to test cycle: Power of components (a), inputs (b), corrected compressor mass flow normalized to surge boundary (c), oxygen excess ratio (d), efficiency (e).

penalization might become necessary, when applied to real-life application. GRAMPC itself utilizes a warm start to realize real time capability. In order to decrease the condition number of the control problem, the *states* $\mathbf{x}$ and *inputs* $\mathbf{u}$ are normalized to their initial value, e.g. $\tilde{x}_i = x_i/x_{i,0} = x_i/x_i(t=0)$. A feasible set of values is selected for the inputs' initial values in the first time step.

## 4. RESULTS

The controller presented in Sec. 3 with the nonlinear reduced-order model described in Sec. 2, is perfomed on the detailed dynamic plant model (see Fig. 2) in MATLAB/Simulink®. The alterations in the plant model in comparison to the model by Pukrushpan et al. (2002) concern the valve and orifices: The nozzles in the supply and return manifolds were changed to orifices (see (9)) and the outlet nozzle was augmented to a valve (see (10)). The subsequent results show a robust controller performance concerning the key aspects (I–IV), despite multiple model simplifications in the controller model.

### 4.1 Power Setting and Component Collaboration

A test sequence of six steps in the reference trajectory $P_{\text{net,dem}}$, ranging from $10\,\text{kW}$ to $52\,\text{kW}$, is passed to the controller. By utilizing the predictive nature of the NMPC, the controller gains knowledge of an upcoming step $T_h = 1\,\text{s}$ in advance and can subsequently prepare for the transient response. Figure 5a shows the results of the control. It can be seen that $P_{\text{net}}$ is set without significant deviation from $P_{\text{net,dem}}$. More concretely, the consumption
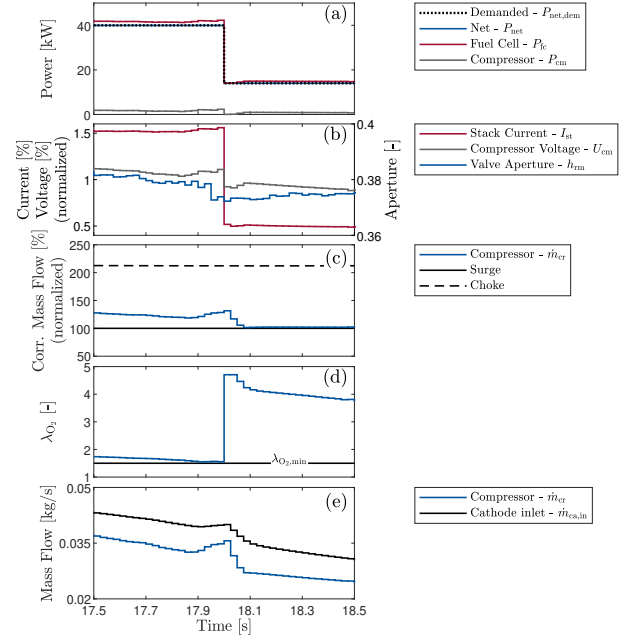


Fig. 6. Controlled system response during step-down at $t = 18\,\text{s}$: Power of components (a), inputs (b), corrected compressor mass flow rate normalized to surge boundary (c), oxygen excess ratio (d), mass flow rates of compressor and cathode inlet (e).

minimization $l_e(\mathbf{x}, \mathbf{u}, t)$ results in a mean absolute deviation of $0.077\,\%$. In particular, the load changes are followed without deviation thanks to the combined consideration of fuel cell and compressor dynamics. The evolution of the inputs $I_{\text{st}}$, $U_{\text{cm}}$ and $h_{\text{rm}}$ is shown in Fig. 5b. Note that $h_{\text{rm}}$ is depicted on a different scale than the other inputs. It can be seen that $I_{\text{st}}$ shows an almost step-like course, resembling $P_{\text{fc}}$, while $U_{\text{cm}}$ and $h_{\text{rm}}$ are noticeably flatter in their response. It can be seen in Fig. 6b that the controller prepares the step-down at $t = 18\,\text{s}$ by leaving the stationary state approximately $0.3\,\text{s}$ before encountering the load change. Immediately before the step, $P_{\text{fc}}$ and $P_{\text{cm}}$ are increased equally, as shown in Fig. 6a. To conclude, evaluating both fuel cell and compressor power simultaneously, enables the controller to set strong load changes with high accuracy.

### 4.2 Compliance with Compressor Boundaries

Figure 5c shows the compressor air mass flow $\dot{m}_{\text{cr}}$ normalized to the mass flows at the surge boundary. $\dot{m}_{\text{cr}}$ is successfully kept between the surge and choke boundary for the entire test sequence. During a step-down in $P_{\text{net,dem}}$, as is shown in Fig. 6c, the compressor temporarily operates close to the surge boundary (18.1-18.5 s). This is because the pressure formation is slower than the mass flow adjustment. Thus, $\dot{m}_{\text{cr}}$ cannot be decreased instantaneously but the flow follows the surge boundary until the pressure reaches the stationary level. Consequently, the dynamic performance of the system is confined by the surge boundary. Since the controller can predict that compressor surge could occur, $\dot{m}_{\text{cr}}$ is increased before the step-down ($t = 17.9\,\text{s}$) in order to widen the distance to the surge boundary. Hence, the predictive nature of the MPC approach enhances the ability for dynamic response.
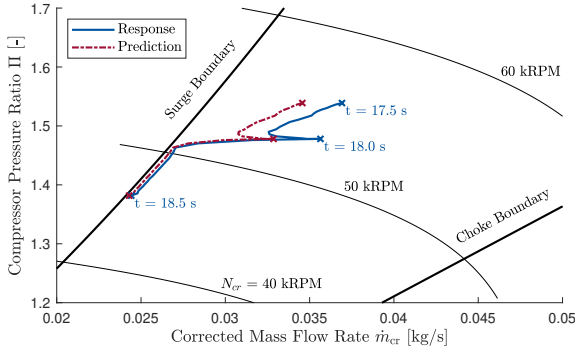
Fig. 7. Corrected compressor mass flow rate trajectory during step-down at $t = 18$ s: Prediction and response (section).

Figure 7 shows the predicted and resulting operation in the compressor map during the step down at $t = 18$ s (compare Fig. 3). It underlines the importance of an accurate approximation of $\dot{m}_{\mathrm{cr}}$ in proximity to the operation boundaries. While far from the boundary a large deviation from the detailed formulation in the plant model is noticeable and acceptable, the approximation quality increases closer to the surge boundary. Neither the prediction nor the detailed model's response violate the constraints.

### 4.3 Obedience of Minimum Oxygen Excess Ratio

Besides satisfying the compressor operation limits, Fig. 5d shows that an oxygen excess ratio above $\lambda_{\mathrm{O_2,min}} = 1.5$ is guaranteed for the entire load sequence. Intuitively, high $P_{\mathrm{net}}$ results in a low $\lambda_{\mathrm{O_2}}$, whereas during a low power demand a vast amount of oxygen is available. While $\lambda_{\mathrm{O_2}}$ returns quickly to a stationary value after step-ups in $P_{\mathrm{net,dem}}$, the relaxation takes longer after severe step-downs (see Fig. 6d), because the compressor is operating at the surge limit and hence cannot immediately reduce $\dot{m}_{\mathrm{cr}}$. It can be seen that $\lambda_{\mathrm{O_2}}$ ranges from 1.6 to 2.4 in steady state for medium loads. Hence, the stationary values of $\lambda_{\mathrm{O_2}}$ resemble the reference values presented in those contributions that use efficiency-oriented excess ratios (Guo et al., 2013; Hähnel et al., 2015).

Especially during intense step-ups, the fuel cell is at risk for oxygen starvation (compare e.g. at $t = 9$ s). In detail, changing the compressor operation ($U_{\mathrm{cm}}$ and hence indirectly $\dot{m}_{\mathrm{cr}}$) does not have an instantaneous impact on the mass flow entering the cathode $\dot{m}_{\mathrm{ca,in}}$ and thus $\lambda_{\mathrm{O_2}}$ (see the time-delayed response in Fig. 6e for an exemplary step-down). Starvation is prevented by using predictive information, and thus by preemptively increasing the supplied mass flows prior to the load change. It is shown that starvation is safely prevented even for step-like power changes without treating $\lambda_{\mathrm{O_2}}$ as an optimization objective.

### 4.4 Fuel Cell System Efficiency and Power Loss

The fuel cell's gross efficiency $\eta_{\mathrm{fc}} = {}^{P_{\mathrm{fc}}}\!/_{P_{\mathrm{H_2}}}$ and the system's net efficiency $\eta_{\mathrm{net}} = {}^{P_{\mathrm{net}}}\!/_{P_{\mathrm{H_2}}}$ are shown in Fig. 5e. Intuitively, $\eta_{\mathrm{fc}}$ is higher than $\eta_{\mathrm{net}}$, since the operation of the compressor consumes a portion of the generated power. Especially during load steps, $\eta_{\mathrm{net}}$ is lowered due to the increased operation of the compressor. Figure 8
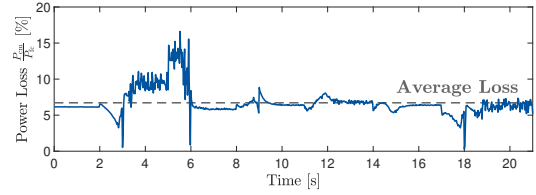


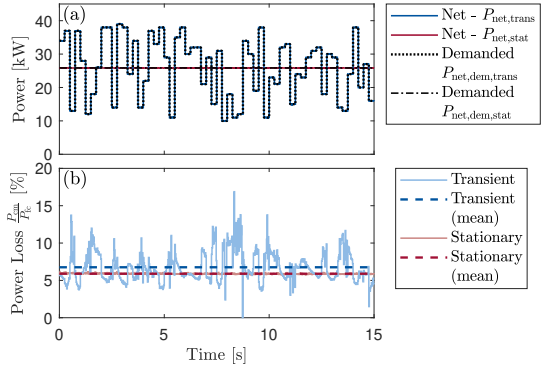Fig. 8. Relative power loss due to compressor operation during test cycle.



Fig. 9. Transient operation versus stationary operation - Net and demanded Power and power loss caused by compressor.

shows the relative power loss ${}^{P_{\mathrm{cm}}}\!/_{P_{\mathrm{fc}}}$ caused by the compressor. On average, the compressor consumes 6.7 % of the generated power, while in one time step the loss rises to approximately 16.6 % in preparation for the step-up (see $t = 5 - 6$ s). Hence, by minimizing the consumption in $l_{\mathrm{e}}(\mathbf{x}, \mathbf{u}, t)$, the loss is reduced both in stationary and in transient operation.

### 4.5 Transient and Stationary Behavior

Finally, a highly transient test sequence is compared to a stationary operation in order to further examine the transient efficiency, as shown in Fig. 9a. The transient sequence $P_{\mathrm{net,dem,trans}}$ consists of randomly distributed power levels between 10 kW and 40 kW, each 250 ms long. The stationary power $P_{\mathrm{net,dem,stat}}$ is chosen to equal the arithmetic mean of the transient cycle. It can be seen that both responses $P_{\mathrm{net,trans}}$ and $P_{\mathrm{net,stat}}$ are indistinguishable from $P_{\mathrm{net,dem,trans}}$ and $P_{\mathrm{net,dem,stat}}$. $P_{\mathrm{net}}$ only deviates 0.049 % from $P_{\mathrm{net,dem}}$ in stationary operation, and 0.066 % during the transient sequence. In particular, the transient load changes are followed without deviation. Moreover, neither the compressor boundaries nor the minimum oxygen excess ratio are violated. The power loss caused by the operation of the compressor is shown in Fig. 9b and resembles the behavior in Fig. 8. Note that the average power loss during the transient cycle is raised from 5.9 % in stationary operation to only 6.8 %. This underlines the controller's ability to enforce efficiency both in transient and stationary operations.

### 4.6 Analysis of Computation Time

The simulations were executed on an Intel® Core™ i5-8250u processor (4x1.6 GHz). Though depending on the specific run, one time step ($\Delta t = 25$ ms) of the sequence in

Fig. 5 was on average simulated in approximately 20.5 ms, which allowed the computation within sampling time. We acknowledge that the computation time might differ when applied to a real-time hardware used in practice. Note, that the performance of the presented NMPC is strongly dependent on parameter tuning. The controller could be further examined to reduce the computational resources.

## 5. CONCLUSION

This paper presents a nonlinear model predictive control (NMPC) for the simultaneous tracking of demanded power and efficiency maximization in a fuel cell system. The presented approach is capable of tracking the power demand without significant deviation or dynamic delay during load changes. In contrast to the majority of contributions, the integration of the compressor power in the optimal control problem enables a joint power setting with the fuel cell. The omission of oxygen excess ratio as a control variable introduces a degree of freedom, which we utilize to further improve the system efficiency in both transient and steady state. Moreover, we prevent oxygen starvation by satisfying an inequality constraint. The presented deduced controller model shows sufficient accuracy to represent the detailed dynamic plant model, while facilitating adequate calculation times. Consequently, the presented NMPC is able to sustainably and robustly operate the system within the boundaries without thereby losing transient performance. Thus, the faster and stronger load changes occur in the power demand, the higher is the benefit of the presented control approach.

Next steps towards real-life application are the implementation of reference planning, the state observer, and the low level-controllers. Moreover, a robustness analysis of the NMPC under prediction disturbances might enhance the controller's real-life performance.

## REFERENCES

Arce, A., del Real, A.J., Bordons, C., and Ramirez, D.R. (2010). Real-time implementation of a constrained mpc for efficient airflow control in a pem fuel cell. *IEEE Transactions on Industrial Electronics*, 57(6), 1892–1905.

Bocklisch, T., Paulitschke, M., and Bocklisch, S. (2010). Modelling and control of a dc/dc-converter system for fuel cell-direct storage-hybrid units. In *International Exhibition and Conference for Power Electronics Intelligent Motion Power Quality*.

Bordons, C., Arce, A., and del Real, A.J. (2006). Constrained predictive control strategies for pem fuel cells. In *American Control Conference, 2006*. IEEE.

Ellis, M., Durand, H., and Christofides, P.D. (2014). A tutorial review of economic model predictive control methods. *Journal of Process Control*, 24(8), 1156–1178.

Englert, T., Völz, A., Mesmer, F., Rhein, S., and Graichen, K. (2019). A software framework for embedded nonlinear model predictive control using a gradient-based augmented lagrangian approach (grampc). *Optimization and Engineering*. URL https://doi.org/10.1007/s11081-018-9417-2.

Ettihir, K., Boulon, L., and Agbossou, K. (2016). Optimization-based energy management strategy for a fuel cell/battery hybrid power system. *Applied Energy*, 163, 142–153.

Gruber, J.K., Bordons, C., and Oliva, A. (2012). Nonlinear mpc for the airflow in a pem fuel cell using a volterra series model. *Control Engineering Practice*, 20(2), 205–217.

Guo, A., Chen, W., Li, Q., Liu, Z., and Que, H. (2013). Air flow control based on optimal oxygen excess ratio in fuel cells for vehicles. *Journal of Modern Transportation*, 21(2), 79–85.

Hähnel, C., Aul, V., and Horn, J. (2015). Power efficient operation of a pem fuel cell system using cathode pressure and excess ratio by nonlinear model predictive control. In *2015 European Control Conference (ECC)*, 3340–3345. IEEE.

Haubrock, J., Heideck, G., and Styczynski, Z. (2006). Electrical efficiency losses occurred by the air compressor for pemfc. *Proceedings of the World Hydrogen Energy Conference WHEC Lyon, France*.

Inukai, J., Miyatake, K., Takada, K., Watanabe, M., Hyakutake, T., Nishide, H., Nagumo, Y., Watanabe, M., Aoki, M., and Takano, H. (2008). Direct visualization of oxygen distribution in operating fuel cells. *Angewandte Chemie (International Edition)*, 47(15), 2792–2795.

Kurz, R., J. Fowler, E., Marechale, R., Cave, M., and Ji, M. (2016). Operation of centrifugal compressors in choke conditions. *Asia Turbomachinery and Pump Symposium*.

Li, C.Y. and Liu, G.P. (2009). Optimal fuzzy power control and management of fuel cell/battery hybrid vehicles. *Journal of Power Sources*, 192(2), 525–533.

Liu, S., Bin, Y., Li, Y., and Scheppat, B. (2018). Hierarchical mpc control scheme for fuel cell hybrid electric vehicles. *IFAC-PapersOnLine*, 51(31), 646–652.

Neisen, V., Baader, F.J., and Abel, D. (2018). Supervisory model-based control using mixed integer optimization for stationary hybrid fuel cell systems. *IFAC-PapersOnLine*, 51(32), 320–325.

Puig, V., Rosich, A., Ocampo-Martinez, C., and Sarrate, R. (2007). Fault-tolerant explicit mpc of pem fuel cells. In *46th IEEE Conference on Decision and Control, 2007*, 2657–2662. IEEE.

Pukrushpan, J.T., Stefanopoulou, A.G., and Peng, H. (2002). University of michigan fuel cell stack simulation package. URL http://hdl.handle.net/2027.42/90423.

Pukrushpan, J.T., Stefanopoulou, A.G., and Peng, H. (2004). *Control of fuel cell power systems: Principles, modeling, analysis and feedback design*. Advances in industrial control. Springer Science & Business Media.

Suh, K.W. and Stefanopoulou, A.G. (2006). Inherent performance limitations of power-autonomous fuel cell system. In *American Control Conference, 2006*. IEEE.

Vahidi, A., Stefanopoulou, A., and Peng, H. (2006). Current management in a hybrid fuel cell power system: A model-predictive control approach. *IEEE Transactions on Control Systems Technology*, 14(6), 1047–1057.

Zhao, D., Li, Y., Huangfu, Y., Dou, M., and Tan, B. (2016). Energy optimization of a pem fuel cell system by minimizing the parasitic consumption generated by the compressor. In *2016 IEEE Transportation Electrification Conference and Expo (ITEC'16)*, 1–4. IEEE.